small methods
www.small-methods.com

Enhanced Discriminability of Viral Vectors in Viscous Nanopores

Makusu Tsutsui, Yuji Tsunekawa, Mikako Wada, Akihide Arima, Azusa Onodera, Masumi Nishina, Miho Nagoya, Yoshinobu Baba, Tomoji Kawai, and Takashi Okada**

Achieving safe and efficient gene therapy hinges upon the inspection of genomes enclosed within individual nano-carriers to mitigate potential health risks associated with empty or fragment-filled vectors. Here solid-state nanopore sensing is reported for identifications of intermediate adeno-associated virus (AAV) vectors in liquid. The method exploits the phenomenon of translocation slowdown induced by the viscosity of salt water-organic mixtures. This enables real-time ionic current measurements allowing precise tracking of the electroosmotic flow-driven motions of recombinant AAV vectors in a nanopore. The resulting ionic signals facilitate discrimination between replicative intermediates carrying ssDNA fragments and its full vector counterparts based on genome length-derived subtle nanometer differences in the viral diameters. This rapid and non-destructive means of genome analysis within virus capsids provides a promising avenue toward a robust methodology for ensuring the integrity of AAV vectors before administration.

1. Introduction

In the ever-evolving landscape of medical science, gene therapeutics has emerged as a formidable ally in not only treating genetic diseases but also in the global fight against pandemic outbreaks.[1–3] Advanced materials for highly efficient vehicles, such as virus vectors, carbon nanomaterials, and lipid proteins, play a pivotal role in enhancing the encapsulation and delivery of therapeutic genomes.[4–6] In particular, AAV vector has proven useful as a safe and effective tool for cancer therapy among the plethora of platforms available to date.[7–9] However, challenges persist in ensuring safety and efficacy, often requiring substantial investments in quality controls.

A critical hurdle lies in inspecting genomes within individual nano-carriers, as the presence of empty or fragment-filled vectors raises concerns about potential side effects upon administration.[10,11] In this regard, ultracentrifugation is utilized as a standard technique for sorting the viral vectors.[12] The atomic resolution of transmission electron microscopy has been exploited for interrogating the presence of genomes in each capsid by images.[13] There are also emerging methods for single-vector analyses such as the nanofluidic resonators[14] and mass photometry[15] for high throughput discriminations of AAVs. Meanwhile, although these analytical procedures can discriminate the empty and full vectors, there are no effective techniques capable of characterizing the replicative intermediates[16] in a non-destructive manner, which requires a sensor that can probe a minute difference in the physical characteristics of the viral particles reflecting the size of the enclosed genomes.

We herein report solid-state nanopore sensing for identifying intact intermediate products of AAVs in salt solution at the single-vector level. A key finding is that the translocation dynamics of AAV particles can be decelerated in an organic-water mixture of high viscosity for the ionic current measurements to finely track their motions. The resulting ionic signals allowed to discern the genome length-derived single-nanometer difference in the diameters of the intermediate AAV vectors without disrupting the capsids.

M. Tsutsui, T. Kawai
The Institute of Scientific and Industrial Research
Osaka University
Mihogaoka 8-1, Ibaraki, Osaka 567-0047, Japan
E-mail: tsutsui@sanken.osaka-u.ac.jp

Y. Tsunekawa, M. Wada, A. Onodera, M. Nishina, M. Nagoya, T. Okada
Division of Molecular and Medical Genetics
Center for Gene and Cell Therapy
The Institute of Medical Science
The University of Tokyo
Tokyo 108-8639, Japan
E-mail: t-okada@ims.u-tokyo.ac.jp

A. Arima, Y. Baba
Research Institute for Quantum and Chemical Innovation
Institutes of Innovation for Future Society
Nagoya University
Nagoya 464-8603, Japan

Y. Baba
Institute of Quantum Life Science
National Institutes for Quantum and Radiological Science and Technology
Anagawa 4-9-1, Inage-ku, Chiba 263-8555, Japan

The ORCID identification number(s) for the author(s) of this article can be found under https://doi.org/10.1002/smtd.202401321

DOI: 10.1002/smtd.202401321

2. Results and Discussion

Electrical detections of recombinant AAV-9 encapsulating single-stranded DNA (ssDNA) of 2599 (Full) and 1491 base long (Intermediate) as well as empty vectors (formed by a procedure reported elsewhere[17,18]) were performed by measuring the ionic current I_{ion} through a 70 nm-sized SiN_x pore under the transmembrane voltage V_b (**Figure 1**a; Figure S1, Supporting Information). Here, it is noticeable that the size of the nanopore is notably larger than the 26 nm-sized icosahedral capsids of AAVs. This is because of the increased likelihood of pore clogging by vector particles during measurements when the pore size is smaller than 70 nm (Figure S2, Supporting Information). As the voltage tends to drop at the nanopore due to the relatively large resistance at the nano-confined space, it generates a focused electric field to induce forces to draw the vector particles into the pore.[19,20] In case of the viral vectors in phosphate-buffered saline containing 1.37 M NaCl added to the *cis* compartment, resistive pulses were observed at positive voltages (Figure 1b) denoting the translocation of the vectors via the electroosmotic flow in the *cis*-to-*trans* direction driven by the counter-cation transport at the negatively-charged SiN_x surface with the minor influence of the electrostatic forces for the weak negative zeta potential of AAV.[21] On the contrary, the ionic current traces were featureless under negative V_b due to the reversed fluid flow that repelled the vectors from the pore.

Close inspections of the resistive pulse waveforms revealed relatively wide pulses with t_d over 70 µs showing almost the same heights irrespective of the widths. This feature is characteristic of decelerated translocation modes of objects involving interactions with the pore wall.[22] The result can be naturally interpreted as the ion blockade characteristics of the vectors precisely reflecting the 25 nm-sized icosahedral capsid structures.[23,24] More importantly, the heights of the wide resistive pulses allow discriminations of AAVs by their genome length-derived nanoscopic differences in size (Figures S3–S5, Supporting Information).[23]

Meanwhile, the majority of the resistive pulses were much weaker tending to have lower heights I_p for those showing narrower widths t_d. The trend is characterized by the linear relationship between I_p and t_d with slopes $\alpha \approx -60$ µA s^{-1} as shown by the scatter plots of the empty and full vectors at $t_d < 70$ µs (Figure 1c). In general, these weak pulse signals at $t_d < 70$ µs would be attributable to impurities smaller than the vectors included in the solution. However, it is difficult to imagine any objects that can give rise to such a narrow distribution of t_d since the translocation time generally varies by more than an order of magnitude due to the stochastic nature of the nanoparticle motion dynamics.[25,26] Alternatively, vectors diffusing through the orifice can cause weak resistive pulses via the involved transient increase in the access resistance.[27] Nevertheless, it is unlikely that the skim-through events can lead to the I_p–t_d dependence observed as they are normally found as faint signals in the ionic current traces.[28] Therefore, it is more rational to ascribe the weak resistive pulses to a consequence of the signal retardation stemming from the excessively fast translocation motions of the vector particles.[25,29] This may come into play when the time constant, which is given by the nanopore chip capacitance C coupled with the resistance outside the pore R, becomes comparable to the translocation time of the objects.[30] While the present pore devices were configured to have reduced capacitance as low as 90 pF through the polyimide coating to achieve the RC time constant of ≈2 µs in the electrolyte buffer of resistivity 0.1 Ωm (Figure S1, Supporting Information),[31] it was not enough for tracking the instantaneous ion blockade phenomena associated with the relatively rapid translocation of single-vectors. The resulting broad I_p distributions make it difficult to discriminate the full and intermediate vectors (Figure 1d; Figure S4, Supporting Information) despite the intrinsic difference in their particle sizes inferred from the difference in the average pulse heights for the long-t_d signals.[24] More critically, it can even render bimodal I_p distributions (Figure S6, Supporting Information) that mislead one to anticipate inclusion of two dissimilar vectors in the solution. Since the pore wall interaction-mediated off-axial translocations are rare cases, it is of crucial importance to find a route toward non-retarded resistive pulse detections of AAVs, which also has been a long-standing issue in nanopore sensing of small particles and molecules.[29,32–34]

Enhancing the temporal resolution of the measurement is a possible way to trace the fast translocation dynamics with less delay.[35] Nonetheless, such an effort inevitably entails increased noise, which is often critical as it cannot be treated by analog/digital filters for they simultaneously distort the ionic signals.[36,37] As an alternative, decelerating the translocation speed of the vectors can be a more promising route[38,39] toward the accurate detections of the resistive pulses for discriminations of the replicative intermediates. In the present study, therefore, we examined the nanopore sensing of single-viral vectors in an organic-water mixture of viscosity η higher than that of water (1.1 mPa•s).[40] Glycerol is an organic solvent of high viscosity (1412 mPa•s) useful as a stabilizer for viral vectors, and hence suitable media for suspending the protein nanocages of AAV.[41] We mixed the glycerol with the phosphate-buffered saline to prepare viscous salt solutions of various η and the ion concentration c. Viral vectors were demonstrated as detectable by the ionic current measurements in the glycerol-water mixtures (Figures S7–S9, Supporting Information), wherein we observed a steady widening of the resistive pulses with increasing η suggestive of the slower translocation motions in the more viscous fluid (**Figure 2**a). At the same time, the I_{ion} signals became weaker due in part to the decreased solution conductivity derived from the diminished mobility of ions by virtue of the elevated viscosity known as Walden's rule.[42]

Notably, the ionic signals tended to exhibit less significant variations under higher viscosities (Figure 2b), which is ascribed to the suppressed influence of the signal delay for the viscous-drag-retarded translocation speed of the vectors.[30,31] To evaluate the contributions of the RC effect, we examined the slopes α in the I_p–t_d plots (Figure 2c). In case when $RC << t_d$, I_p is anticipated to change little by t_d, and hence $\alpha \approx 0$. On the contrary, the resistive pulses become weaker for fast-moving vectors when $RC > t_d$, resulting in larger α. While the impact of the enhanced viscosity appeared as the shifting of the data toward longer t_d with increasing η, we also found α to become smaller and level off at $\eta > 5$ mPa•s manifesting the sufficiently slow translocation dynamics in the highly viscous salt solutions with respect to the temporal resolution of the I_{ion} tracing (Figure 2d).[30] As a result, the I_p histograms turned from bimodal to monomodal distributions (Figure 2e) correctly reflecting the well-defined nanoscopic

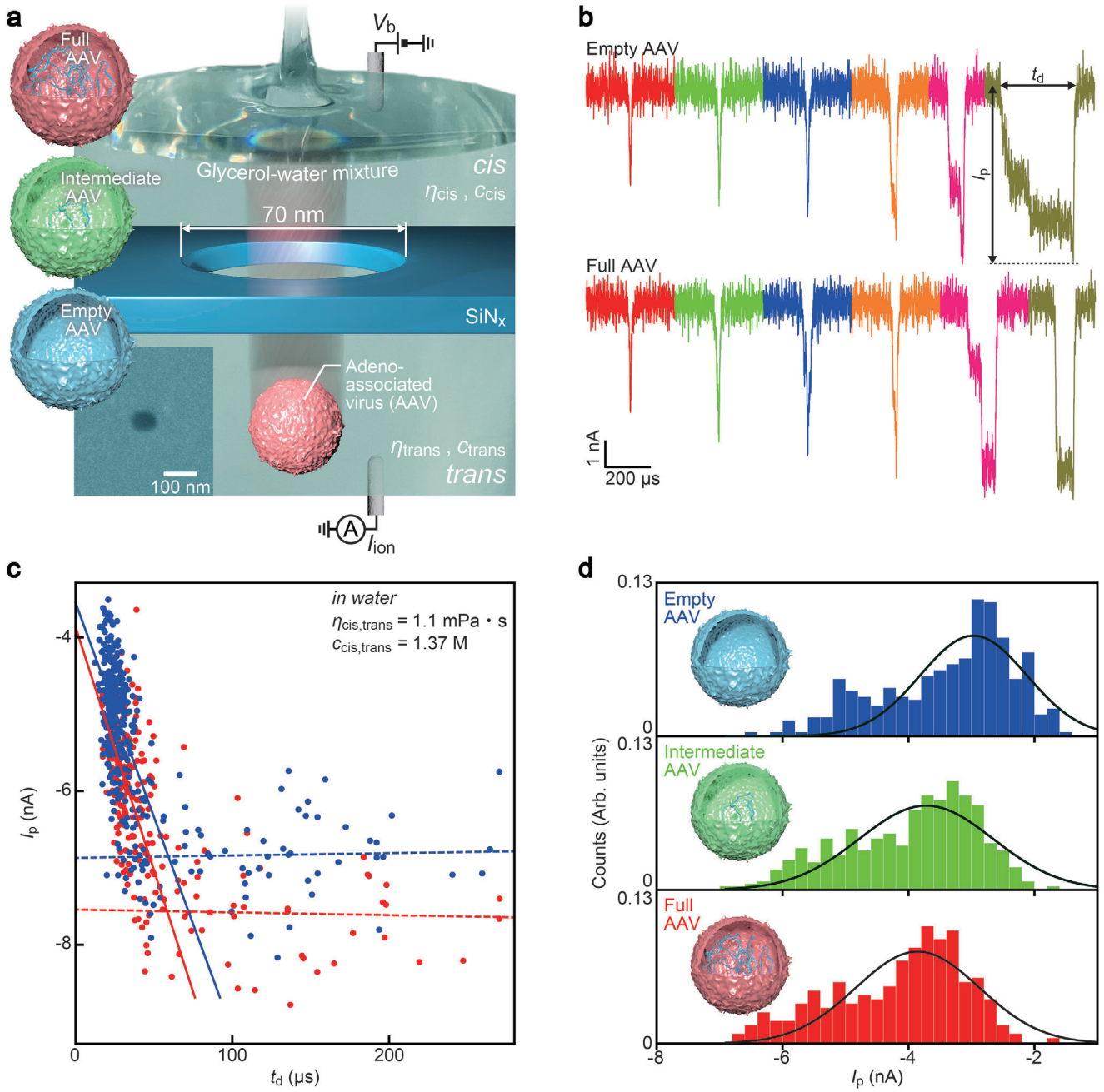

Figure 1. Nanopore sensing of adeno-associated viruses in a viscous nanopore. a) Schematic model depicting resistive pulse detections of AAV vectors encapsulating 2599 base ssDNA (full), 1491 base ssDNA (intermediate), and no genome (empty) in glycerol-salt water mixtures of ion concentration $c_{cis,trans}$ and viscosity $\eta_{cis,trans}$ at the *cis* and *trans* compartments under the transmembrane voltage V_b. The ionic current I_{ion} drops every time when a vector particle passes through the pore via the electroosmotic flow. The inset shows a false-colored scanning electron micrograph of a 70 nm diameter nanopore used for the single-virus detections. b) The ionic current traces displaying resistive pulse signals of empty (top) and full (bottom) vectors. I_p and t_d denote the signal height and width, respectively (V_b = 0.3 V). Narrower resistive pulses tend to have lower heights suggesting inadequate time resolution of the measurement configuration to track the temporal ion blockades upon the fast translocation of the AAV vectors. c) I_p versus t_d scatter plots of the resistive pulses obtained for empty (blue) and full (red) AAV. Solid and dashed lines are linear fittings to the plots in the short (< 70 µs) and long (>70 µs) t_d regimes, respectively. d) Broad I_p distributions of full (red), intermediate (green), and empty (blue) vectors dignifying the pronounced influence of signal blunting on the resistive pulse heights. Solid curves are Gaussian fits exhibiting large overlaps among the three types of AAV measured.

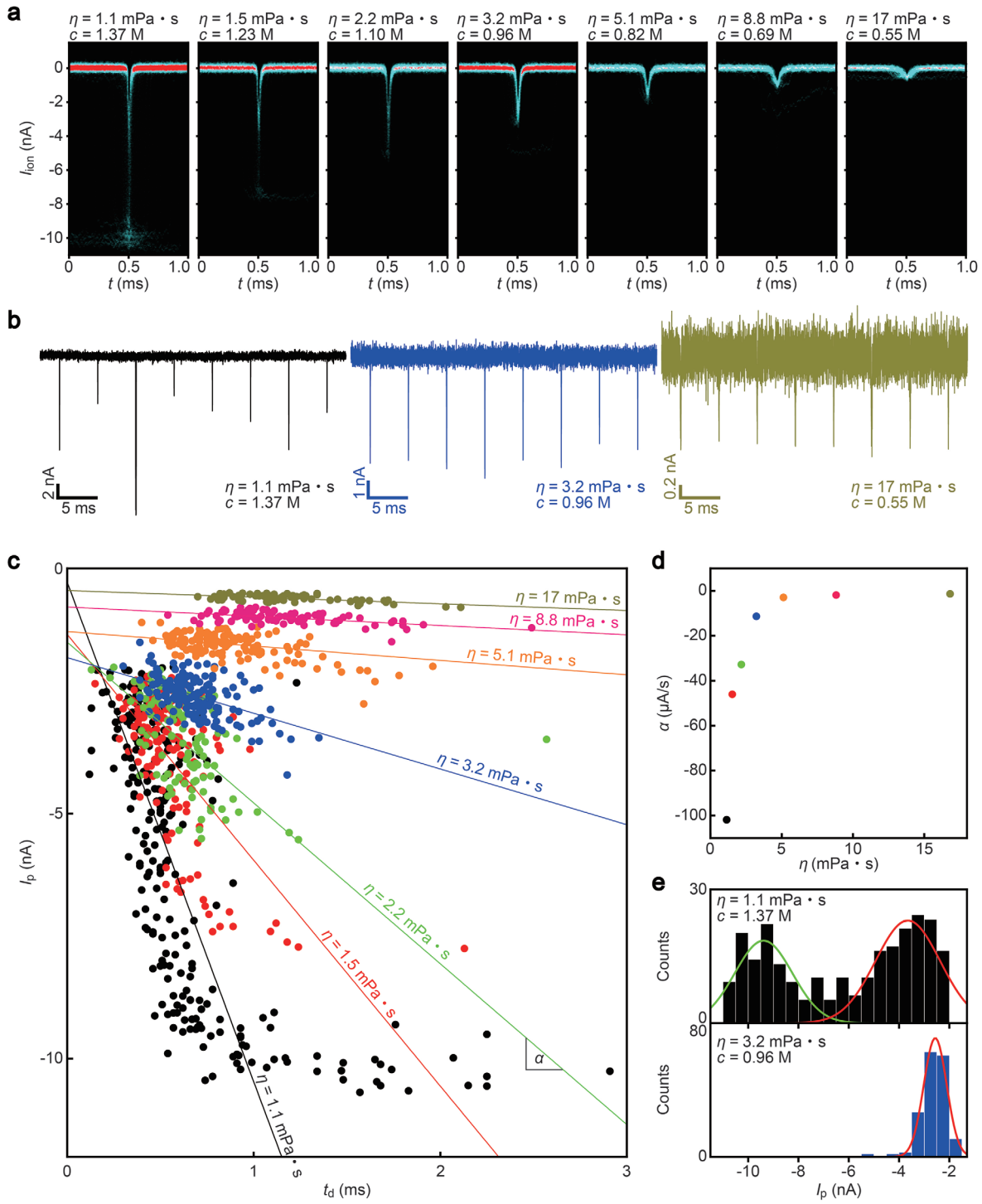

Figure 2. Slowing down translocation in a viscous nanopore. a) Resistive pulses of empty vectors measured in glycerol-water mixtures of various salinity c and viscosity η ($V_b = 0.3$ V). Wider resistive pulses were detected under enhanced viscosity suggesting lower translocation speed of the vectors via the slower electroosmotic flow. Moreover, the signals became weaker under larger η due to the decreased mobility of ions in the more viscous solutions. b) Partial ionic current traces at 1.1 (black), 3.2 (blue), and 17 mPa•s (dark yellow). The variations in the signal heights are suppressed at larger η for the less impact of the signal blunting. Meanwhile, the excessively high viscosity involves lower ionic conductivity that leads to a diminished signal-to-noise ratio. c) I_p plotted against t_d for the resistive pulses recorded in the glycerol solutions of $\eta = 1.1$ (black), 1.5 (red), 2.2 (green), 3.2 (blue), 5.1 (orange), 8.8 (pink), and 17 mPa•s (dark yellow). Solid lines are linear fittings whose slopes α denote the contributions of the signal retardations. d) Solution viscosity dependence of α. Color code is the same as that in c). e) I_p histograms at $\eta = 1.1$ (black) and 3.2 mPa•s (blue). Solid curves are Gaussian fits. The bimodal I_p distribution at 1.1 mPas is attributed to the blunted signals of low I_p included in the data. In contrast, the single-peak histogram at 3.2 mPa•s suggests less influence of the signal blunting for the retarded translocation dynamics of the vectors in the more viscous fluid.

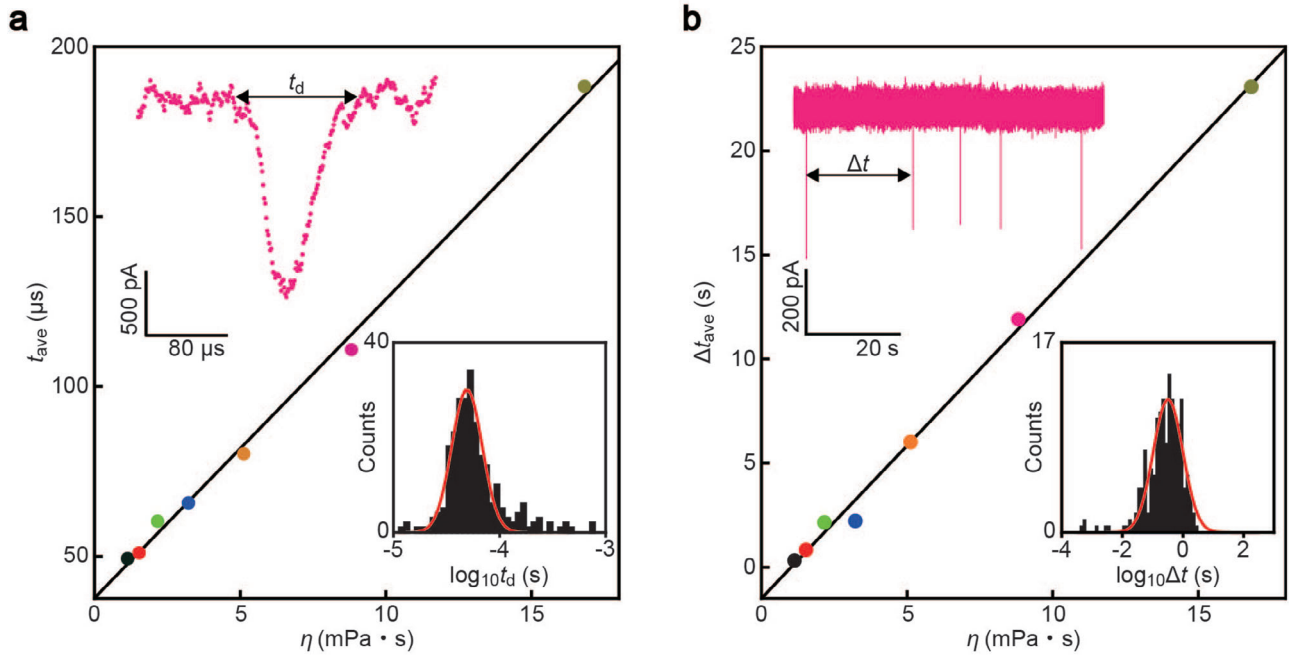

Figure 3. AAV detection throughput. a,b) The average resistive pulse width t_{ave} a) and the intervals Δt_{ave} between two consecutive resistive pulses b) plotted against η. The data are deduced from Gaussian fittings to the t_d and Δt distributions. Solid lines are linear fittings. The linear rises in t_d and Δt are a direct cause of the lowered electroosmotic flow velocity under larger viscosity.

structures of the vector capsids. The viscous nanopore approach is, therefore, effective for reliable detection of viral vectors.

It should be noted that the fluid viscosity enhancement for the translocation motion slowdown involves ion mobility reduction as evidenced by the concomitant decrease in the open pore current I_0 and I_p. On the other hand, the root-mean-square noise I_{noise} changes only a little, causing the ratio I_p/I_{noise} to decrease with η (Figure S10, Supporting Information). Thus, care should be taken to avoid excessively high viscosity as it unnecessarily degrades the signal intensities to impair the single-vector sensitivity of the nanopore sensing.

The retarded motions of the vectors are quantitatively evaluated by a statistical analysis of the resistive pulse widths. The logarithmic t_d showed monomodal distributions (Figure S11, Supporting Information), which were fitted by Gaussian peaks to assess the average translocation time t_{ave} (**Figure 3a** inset). Plotting against η, t_{ave} revealed a linear dependence on the solution viscosity (Figure 3a). Theoretically, the electroosmotic flow velocity v_{EOF} at the nanopore under the electric field E is roughly described as $\varepsilon\zeta_w E/\eta$ with the solution permeability ε and the zeta-potential ζ_w at the SiN_x wall.[19] In the measurements, the vectors were observed to move along the fluid flow, thus anticipating their translocation speed v_{vec} to be equivalent to v_{EOF}.[19] Since $v_{vec} \approx {t_{ave}}^{-1}$, therefore, it predicts $t_{ave} \approx \eta$ seen for the electroosmosis-driven AAV (Figure 3a).

The capture rates of vectors are a direct measure of the detection throughput, which can be assessed from the time interval Δt between two consecutive resistive pulses.[43] Δt varied widely demonstrating the stochastic nature of the capture-to-translocation dynamics. To characterize its dependence on the solution viscosity, the average interval Δt_{ave} was calculated from the statistical distributions (Figure S12, Supporting Information). Analogous to the translocation time, Δt_{ave} scaled linearly with η as expected from the fact that the AAV is carried by the electroosmotic flow. More precisely, the volume flow rate V_f is described as $V_f = v_{EOF} A_{pore}$ with the cross-sectional nanopore area A_{pore} of $\pi {d_{pore}}^2/4$. Under the given concentration of the vectors c_{AAV}, therefore, the capture rate f_{cap}, i.e., the number of particles passing through the nanopore per unit time, is described as $f_{cap} = V_f c_{AAV}$. This anticipates $\Delta t_{ave} \approx \eta$ as observed in Figure 3b from $f_{cap} = {\Delta t_{ave}}^{-1}$ and $V_f \approx \eta^{-1}$, highlighting the fact that the slow translocation comes at a price of reduced detection rates (Figure S13, Supporting Information).

We add to note that it is not straightforward to control the vector speed and the capture rate by the transmembrane voltage. This is because of the concurrent changes in the electrostatic forces on the vectors with V_b that may even induce oscillation modes of vector motions under the balanced electrophoretic and hydrodynamic drag forces (Figure S14, Supporting Information).

In this regard, it is of interest to explore whether a viscosity gradient can be useful in tailoring the translocation dynamics of the vectors.[39,44] Settling $\eta_{cis} < \eta_{trans}$, for instance, the vectors in the *cis* compartment are expected to diffuse more efficiently potentially leading to higher f_{cap}. To verify this, we performed the resistive pulse measurements under positive (η_{cis} = 1.1 mPa•s / η_{trans} = 3.2 mPa•s) and negative (η_{cis} = 3.2 mPa•s/η_{trans} = 1.1 mPa•s) viscosity difference. The signal profiles exhibited slower (faster) changes of I_{ion} at the onsets than at the tails under the negative (positive) gradients reflecting the lower (higher) mobility of the vectors at the *cis*-side of the orifice (**Figure 4a,b**). The viscosity dependence of the translocation dynamics can be seen more clearly in the partial signal widths at the onsets (t_{on}) and tails (t_{off}), where the additions of glycerol to *cis* (*trans*) led to more pronounced elongations of t_{on} (t_{off}) (Figure 4c; Figures S15,S16,

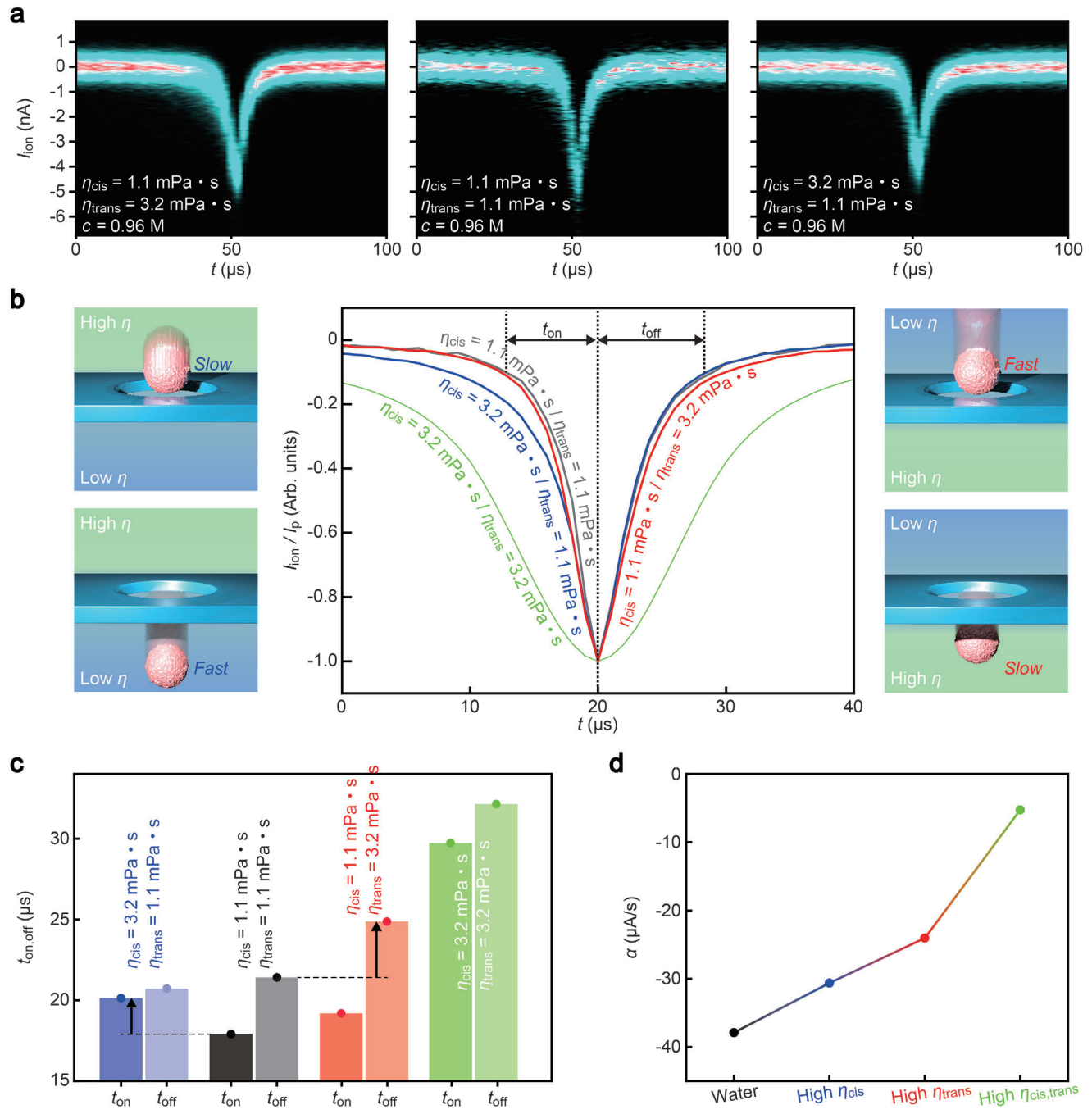

Figure 4. Vector translocation dynamics under viscosity gradients. a) Resistive pulses of full vectors detected under $\eta_{cis} > \eta_{trans}$ (left), $\eta_{cis} = \eta_{trans}$ (middle), and $\eta_{cis} < \eta_{trans}$ (right) with the viscosities arranged to be either 1.1 mPa•s or 3.2 mPa•s (V_b = 0.3 V). b) Average resistive pulses under $\eta_{cis} > \eta_{trans}$ (blue), $\eta_{cis} = \eta_{trans}$ (green), and $\eta_{cis} < \eta_{trans}$ (red). The case in water is also shown as a black curve. The lower curvatures at the onsets (tails) of the ionic signals signify the relatively lower mobilities of the vector particles in the *cis* (*trans*) compartments of higher viscosity. t_{on} and t_{off} are the widths at the onsets and tails of the resistive pulses depicting the speed of the viral vectors at the entrance and exit of the nanopore, respectively. Green curve is the average signal in case when *cis* and *trans* compartments were filled with glycerol-water mixture of 3.2 mPa•s. c) Average t_{on} and t_{off}. The increase in the viscosity at *cis* and *trans* elongates t_{on} and t_{off}, respectively, as shown by the arrows. Note the longest $t_{on,off}$ when the viscosity was high at both sides of the nanopore (green). d) α becomes sufficiently small when $\eta_{cis,trans}$ = 3.2 mPas.

Supporting Information). While it anticipates faster diffusion motions of the vectors under $\eta_{cis} < \eta_{trans}$, on the other hand, we found little difference in f_{cap} under the positive and negative η gradients (Figure S17, Supporting Information). This is ascribed to the fact that the local viscosity at the nanopore changes little irrespective of the viscosity differences.[45,46] As a result, it provided similar fluid flow rates via electroosmosis under the applied transmembrane voltage to draw the vectors into the nanopore. Consistently, the overall effects of the viscosity gradients on the translocation speed (Figures S18, Supporting Information) were also found as marginal for the resulting low in-pore viscosity compared to the case when homogeneously increasing the viscosity at both sides of the membrane (as also appeared in the open pore current (Figure S19, Supporting Information)).[45,46] Eventually, η gradient approach is found as not useful for enhancing the temporal resolution of the nanopore sensing (Figure 4d).

Finally, we evaluate the discriminability of the AAV in the viscous nanopore. Because of the weak impact of viscosity gradients on translocation speed, a significant portion of vectors traversed the nanopore rapidly characterized by transit times less than 40 μs and corresponding α below -20 μA s^{-1} (**Figure 5a**). The rapid modes of translocation resulted in considerable signal blunting, leading to significant overlap in the I_p–t_d plots for full, empty, and intermediate AAV-9 particles. In contrast, the vector motions can be slow-downed by raising the viscosity homogeneously to $\eta_{cis,trans}$ = 3.2 mPa•s enabling t_d > 40 μs with $\alpha \approx -2$ μA s^{-1} (Figure 5b). This allowed the less overlaps of the I_p distributions among the three types of vectors (Figure 5c,d). To assess the distinguishability, we calculated the resolution $\beta = 1.18(I_1 - I_2)/(w_1 - w_2)$ of the Gaussian peaks fitted to the I_p histograms of two AAV, where $I_{1,2}$ and $w_{1,2}$ are their center and the full width at half maximum, respectively (Figure 5e)). In water, the nanoscopic difference in the sizes of the full and the intermediate vectors are scarcely discernible due to the signal blunting resulting in β near 0. Adding glycerol to *cis*, β is found to be enhanced slightly to ≈0.1 by virtue of the reduced α for the retarded translocation dynamics. The discriminability further improved to $\beta > 0.4$ by the additional reduction in the vector speed with glycerol in both *cis* and *trans* (Figure 5f), thus proving the capability of the viscous nanopore sensing for not only counting empty and full vectors but also identifying intermediates (see also Figure S20, Supporting Information for the results of AAV9 carrying longer ssDNA).

3. Conclusion

Solid-state nanopore sensing in organic-water mixtures is demonstrated as capable of discriminating full, empty, and intermediate AAV vectors in label-free and non-destructive fashion. Meanwhile, the present study revealed the importance to arrange the viscosity with respect to the given temporal resolution of the nanopore sensors. Specifically, more viscous liquid serves to render slower translocation speed for mitigating the signal attenuation. At the same time, however, it weakens the I_{ion} signatures due to the enlarged ionic resistance thereby reducing the signal-to-noise ratio. Capture rate is another issue since the elevated viscosity lowers the mobility of the vectors outside the pores. Consequently, selecting an optimal viscosity requires balancing these trade-offs to achieve effective discrimination of targeted vectors in specific media.

There are other methods demonstrated to effectively slow the translocation of objects by increasing solution viscosity. One such approach is macromolecular crowding, which can significantly enhance the local viscosity within nanopores.[44,47–49] A key advantage of modulating local viscosity is that it maintains high mobility of analytes outside the pore, thereby preventing a significant reduction in capture rates compared to the case of changing the viscosity of entire solution. However, random nanofluidic networks within gels limit their direct application for nanopore sensing of relatively large nanoparticles, such as AAV vectors, as these are likely to be blocked at the gel surface. In contrast, the proposed method offers greater versatility, making it applicable to analytes of various sizes.

Looking ahead, it is pointed out that while the deteriorated capture rate is unavoidable under the enhanced viscosity, there are countermeasures already proven effective to keep the detection throughput high such as on-chip amplifications[50] and multipore detections.[51] In addition, further improvement in the vector discriminability can be expected by membrane material designs[52] and surface engineering[53] to render lower charge density at the pore wall for gaining higher signal intensities with slower translocation motions via the moderate electroosmotic flow under larger transmembrane voltages. Leveraging post-digital analyses by machine learning of resistive pulse profiles[54,55] would also serve to enhance the ability to discern the subtle difference in the physical features of individual vectors carrying genomes of various lengths. Besides the issues related to the resistive pulse analyses, it is of importance to establish an efficient method for purifying the crude AAV products as they contain various impurities such as small proteins that can clog nanopores during the resistive pulse detections. In this regard, multipore filters[56] and in situ, ultracentrifugation mechanism[57] can be useful for separating non-vector particles and molecules on chip. Being a compact sensor of a simple structure for detecting intact vectors at a single-particle level, it paves the way for enhanced quality control of AAV products in gene therapy applications.

4. Experimental Section

Fabrication of SiN_x Nanopores: A 4-inch Si wafer was coated with 50 nm-thick SiN_x layers on both sides by low-pressure chemical vapor deposition followed by dicing into 25 mm chips by a dicer. A 1 mm square region of the SiN_x was removed by reactive ion etching using CHF_3 etchant gas through a metal mask. The exposed Si was wet-etched in KOH aq. heated at 80 degrees Celsius on a hot plate. This created a pyramidal-shaped deep trench with a 40 nm-thick SiN_x membrane of ≈100 μm × 100 μm size at the bottom. Electron beam resists (ZEP520A) were spin-coated on the membrane side of the surface and baked at 180 degrees Celsius on a hot plate. A circle of 70 nm diameter was delineated at the center of the membrane by electron beam lithography. After development, the residual resist layer was used as a mask to open a 70 nm diameter pore in the membrane by the reactive ion etching process. The chip was then kept in *N*,*N*-dimethylformamide overnight to dissolve the resist film and subsequently rinsed with ethanol and acetone.

Nanopore Chip Coatings: The membrane side of the nanopore chip surface was spin-coated with a photo-sensitive polyimide precursor and prebaked on a hot plate. A 50 μm circle around the nanopore was delineated in the 5 μm-thick layer by light emission diode lithography. The photo-irradiated region was dissolved in a remover solution to create a microwell. Subsequently, the chip was heated on a hot plate for the polymerization of the imide layer. On the top of the polyimide, a 20 nm thick

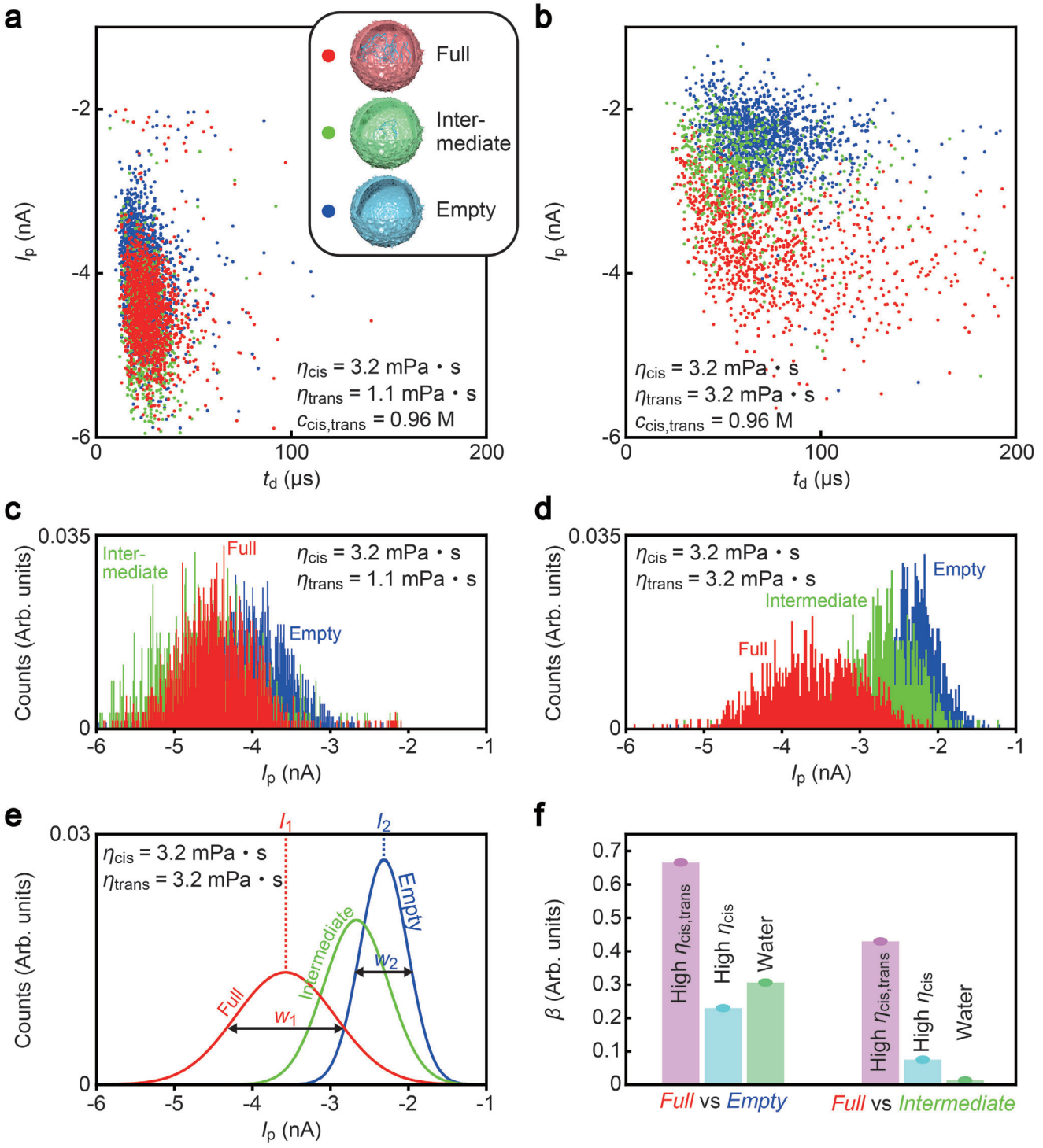

Figure 5. Discriminability of AAV in a viscous nanopore. a) I_p versus t_d scatter plots with a viscosity gradient (η_{cis} = 3.2 mPa•s, η_{trans} = 1.1 mPa•s) under V_b of 0.3 V. The plots of full (red), intermediate (green), and empty AAV (blue) largely overlap due to the short translocation time of ≈ 20 μs. b) When $\eta_{cis,trans}$ = 3.2 mPa•s, t_d becomes longer than 40 μs thereby weakening the influence of signal retardation. c,d) As a result, whereas the three vectors are hardly distinguishable from the I_p distributions when adding glycerol to only *cis* c), they become more separated under $\eta_{cis,trans}$ = 3.2 mPa•s d). e) Gaussian distributions fitted to d). $I_{1,2}$ and $w_{1,2}$ denote the peak centers and the full widths at half maxima, respectively, of the two distributions, which gives the discriminability $\beta = 1.18(I_1 - I_2)/(w_1 - w_2)$ when $I_1 > I_2$. f), Vector discriminability. β becomes high when $\eta_{cis,trans}$ = 3.2 mPa•s allowing discrimination between full and intermediate AAV by the resistive pulse heights.

SiO_2 layer was deposited by chemical vapor deposition excluding the microwell to leave the SiN_x nanopore uncoated and maintain its original size. This SiO_2 film served to enable the eternal bonding of the polydimethylsiloxane (PDMS) flow cell for the ionic current measurements.

Flow Cell Attachments: A mold was prepared for forming PDMS cells by spin-coating a 4-inch silicon wafer with SU-8 photoresist. I-shaped patterns were created via photolithography, followed by post-baking and development in isopropanol. PDMS precursor (Sylgard 184) was poured onto the SU-8 mold in a Petri dish and then cured at 90 degrees Celsius for 2 h in an oven. A 20 mm-sized block was cut using a surgical knife, and three holes were made for injecting sample solution into the nanopore and placing an electrode for ionic current measurements. The PDMS block, featuring an I-shaped trench, was exposed to oxygen plasma alongside a nanopore chip in a chamber for surface activation. Subsequently, the PDMS block was bonded to the nanopore chip externally. This process was repeated to attach another PDMS block on the trench side of the nanopore chip.

Ionic Current Measurements: Electrolyte solutions were poured into the nanopore through the holes in the PDMS flow cells attached to both sides of the chip. Ag/AgCl rods were inserted in one of the three holes in each PDMS block. One rod is connected to a battery-powered potentiostat for applying the transmembrane voltage V_b. The other Ag/AgCl electrode was wired to a custom-designed current amplifier backed by a fast digitizer (PXI NI-5922, National Instruments) and a solid-state drive (HDD-8261) for recording the ionic current at 1 MHz under a program coded in LabVIEW.

Resistive Pulse Extractions: The drifting open pore current was calibrated to zero by removing the linearly-fitted component from the raw data in 0.5-second intervals. Resistive pulse peaks were detected by identifying local minima below a predefined threshold in the offset ionic current traces. Following this, 2.5 milliseconds of data before and after each resistive pulse peak were extracted and saved in a separate file. All the digital processing was conducted using a Visual Basic program.

Supporting Information

Supporting Information is available from the Wiley Online Library or from the author.

Acknowledgements

This work was supported by the Japan Agency for Medical Research and Development (AMED) with the grant numbers 23bm1523001h0002 and 24bm1523007h0002 and the Japan Society for the Promotion of Science (JSPS), London, KAKENHI grant numbers 22H01926, 24K01511, and 24H00646.

Conflict of Interest

The authors declare no conflict of interest.

Author Contributions

M.T., Y.T., M.W., and A.A. contributed equally to this work. All the authors reviewed the manuscript.

Data Availability Statement

The datasets generated during and/or analyzed during the current study are available from the corresponding authors on reasonable request.

Keywords

electrochemistry, virus vector, gene therapy, nanofluidics, nanopore

Received: August 21, 2024
Revised: December 8, 2024
Published online:

[1] E. Rohner, R. Yang, K. S. Foo, A. Goedel, K. R. Chien, *Nat. Biotechnol.* **2022**, *40*, 1586.
[2] A. Raguram, S. Banskota, D. R. Liu, *Cell* **2022**, *185*, 2806.
[3] N. Sayed, P. Allawadhi, A. Khurana, V. Singh, U. Navik, S. K. Pasumarthi, I. Khurana, A. K. Banothu, R. Weiskirchen, K. Bharani, *Life Sci.* **2022**, *294*, 120375.
[4] E. W. Kavanagh, J. J. Green, *Adv. Health. Mater.* **2022**, *23*, 2102145.
[5] K. Bulaklak, C. A. Gersbach, *Nat. Commun.* **2020**, *11*, 5820.
[6] Y. K. Sung, S. W. Kim, *Biomat. Res.* **2019**, *23*, 8.
[7] D. Wang, P. W. L. Tai, G. Gao, *Nat. Rev. Drug. Discovery* **2019**, *18*, 358.
[8] S. Russell, J. Bennett, J. A. Wellman, D. C. Chung, Z.-F. Yu, A. Tillman, J. Wittes, J. Pappas, O. Elci, S. McCague, D. Cross, K. A. Marshall, J. Walshire, T. L. Kehoe, H. Reichert, M. Davis, L. Raffini, L. A. George, F. P. Hudson, L. Dingfield, X. Zhu, J. A. Haller, E. H. Sohn, V. B. Mahajan, W. Pfeifer, M. Weckmann, C. Johnson, D. Gewaily, A. Drack, E. Stone, et al., *Lancet* **2017**, *390*, 849.
[9] E. Mercuri, F. Muntoni, G. Baranello, R. Masson, O. Boespflug-Tanguy, C. Bruno, S. Corti, A. Daron, N. Deconinck, L. Servais, V. Straub, H. Ouyang, D. Chand, S. Tauscher-Wisniewski, N. Mendonca, A. Lavrov, *Lancet Neurol.* **2021**, *20*, 832.
[10] H. Meng, M. Sorrentino, D. Woodcock, C. O'Riordan, V. Dhawan, M. Verhagen, C. Davies, *Hum. Gene Ther.* **2022**, *33*, 202.
[11] M. Muhuri, Y. Maeda, H. Ma, S. Ram, K. A. Fitzgerald, P. W. L. Tai, G. Gao, *J. Clin. Invest.* **2021**, *131*, 143780.
[12] B. Burnham, S. Nass, E. Kong, M. Mattingly, D. Woodcock, A. Song, S. Wadsworth, S. H. Cheng, A. Scaria, R. O'Riordan, *Hum. Gene Ther. Methods* **2015**, *26*, 228.
[13] S. Subramanian, A. C. Maurer, C. M. Bator, A. M. Makhov, J. F. Conway, K. B. Turner, J. H. Marden, L. H. Vandenberghe, S. L. Hafenstein, *Hum. Gene Ther. Methods* **2019**, *30*, 1449.
[14] G. Katsikis, I. E. Hwang, W. wang, V. S. Bhat, N. L. McIntosh, O. A. Karim, B. J. Blus, S. Sha, V. Agache, J. M. Wolfrum, S. L. Springs, A. J. Sinskey, P. W. Barone, R. D. Braatz, S. R. Manalis, *Nano Lett.* **2022**, *22*, 1511.
[15] D. Wu, P. Hwang, T. Li, G. Piszczek, *Gene Ther.* **2022**, *29*, 691.
[16] J. Wang, J. Xie, H. Liu, W. Xiao, *Proc. Natl. Acs. Sci.* **2007**, *104*, 13104.
[17] H. C. Verdera, K. Kuranda, F. Mingozzi, *Mol. Ther.* **2020**, *28*, 723.
[18] T. Tomono, Y. Hirai, H. Okada, Y. Miyagawa, K. Adachi, S. Sakamoto, Y. Kawano, H. Chono, J. Mineno, A. Ishii, T. Shimada, M. Onodera, A. Tamaoka, T. Okada, *Mol. Ther. Methods Clin. Dev.* **2018**, *11*, 180.
[19] M. Firnkes, D. Padone, J. Knezevic, M. Doblinger, U. Rant, *Nano Lett.* **2010**, *10*, 2162.
[20] B. I. Karawdeniya, Y. M. N. D. Y. Bandara, A. I. Khan, W. T. Chen, H.-A. Vu, A. Morshed, J. Suh, P. Dutta, M. J. Kim, *Nanoscale* **2020**, *12*, 23721.
[21] B. Geers, I. Lentacker, A. Alonso, N. N. Sanders, J. Demeester, S. Meairs, S. C. De Smedt, *Mol. Pharmaceutics* **2011**, *8*, 2244.
[22] S. Garaj, S. Liu, J. Golovchenko, D. Branton, *Proc. Natl. Acad. Sci* **2013**, *110*, 12192.
[23] T. F. Lerch, J. K. O'Donnell, N. L. Meyer, Q. Xie, K. A. Taylor, S. M. Stagg, M. S. Chapman, *Structure* **2012**, *20*, 1310.
[24] M. Tsutsui, M. Wada, A. Arima, Y. Tsunekawa, T. Sasaki, K. Sakamoto, K. Yokota, Y. Baba, T. Kawai, *ACS Nano* **2024**, *18*, 15695.
[25] Y. M. Nuwan, D. Y. Bandara, K. J. Freedman, *ACS Nano* **2022**, *16*, 14111.
[26] K. Chen, I. Jou, N. Ermann, M. Muthukumar, U. F. Keyser, N. A. Bell, *Nat. Phys.* **2021**, *17*, 1043.
[27] D. M. Vlassarev, J. A. Golovchenko, *Biophys. J.* **2012**, *103*, 352.

[28] Y. M. Nuwan, D. Y. Bandara, J. Saharia, B. I. Karawdeniya, J. T. Hagan, J. R. Dwyer, M. J. Kim, *Nanotechnology* **2020**, *31*, 335707.
[29] C. Plesa, S. W. Kowalczyk, R. Zinsmeester, A. Y. Grosberg, Y. Rabin, C. Dekker, *Nano Lett.* **2013**, *13*, 658.
[30] J. D. Uram, K. Ke, M. Mayer, *ACS Nano* **2008**, *2*, 857.
[31] M. Tsutsui, K. Yokota, A. Arima, W. Tonomura, M. Taniguchi, T. Washio, T. Kawai, *ACS Appl. Mater. Interfaces* **2018**, *10*, 34751.
[32] J. K. Rosenstein, M. Wanunu, C. A. Merchant, M. Drndic, K. Shepard, *Nat. Methods* **2012**, *9*, 487.
[33] J. Larkin, R. Y. Henley, M. Muthukumar, K. Rosenstein Jacob, M. Wanunu, *Biophys. J.* **2014**, *106*, 696.
[34] J. Y. Y. Sze, A. P. Ivanov, A. E. G. Cass, J. B. Edel, *Nat. Commun.* **2017**, *18*, 1552.
[35] C.-Y. Lin, R. Fotis, Z. Xia, K. Kavetsky, Y.-C. Chou, D. J. Miedzwiecki, M. Biondi, F. Thei, M. Drndic, *Nano Lett.* **2022**, *22*, 8719.
[36] S. Shekar, C.-C. Chien, A. Hartel, P. Ong, O. B. Clarke, A. Marks, M. Drndic, K. L. Shepard, *Nano Lett.* **2019**, *19*, 1090.
[37] M. Tsutsui, T. Takaai, K. Yokota, T. Kawai, T. Washio, *Small Methods* **2021**, *5*, 2100191.
[38] J. Feng, K. Liu, R. D. Bulushev, S. Khlybov, D. Dumcence, A. Kis, A. Radenovic, *Nat. Nanotechnol.* **2015**, *10*, 1070.
[39] S. Confederat, S. Lee, D. Vang, D. Soulias, F. Marcuccio, T. I. Peace, M. A. Edwards, P. Strobbia, D. Samanta, C. Walti, P. Actis, *Small* **2024**, *20*, 2305186.
[40] D. Fologea, J. Uplinger, B. Thomas, D. S. McNabb, J. Li, *Nano Lett.* **2005**, *5*, 1734.
[41] M. A. Croyle, X. Cheng, J. M. Wilson, *Gene Ther.* **2001**, *8*, 1281.
[42] E. Szwajczak, A. Szymanski, *Mol, Cryst. Liq. Cryst.* **1986**, *139*, 253.
[43] M. Charron, K. Briggs, S. King, M. Waugh, V. Tabbard-Cossa, *Anal. Chem.* **2019**, *91*, 12228.
[44] C. C. Chau, S. E. Radford, E. W. Hewitt, P. Actis, *Nano Lett.* **2020**, *20*, 5553.
[45] Y. Qiu, Z. S. Siwy, M. Wanunu, *Anal. Chem.* **2019**, *91*, 996.
[46] M. Tsutsui, K. Yokota, Y. He, T. Kawai, *Small Methods* **2022**, *6*, 2200761.
[47] A. Pluen, P. A. Netti, R. K. Jain, D. A. Berk, *Biophys. J.* **1999**, *77*, 542.
[48] A. Hubarevich, J.-A. Huang, G. Giovannini, A. Schirato, Y. Zhao, N. Maccaferri, De Angelis, F., A. Alabastri, D. Garoli, *J. Chem. Phys.* **2020**, *C 124*, 22663.
[49] F. Yao, K. Peng, Z. SU, L. Tian, Y. Guo, X.-F. Kang, *Anal. Chem.* **2020**, *92*, 3827.
[50] J. D. Spitzberg, X. F. van Kooten, M. Bercovici, A. Meller, *Nanoscale* **2020**, *12*, 17805.
[51] N. B. Athreya, A. Sarathy, J.-P. Leburton, *ACS Sens.* **2018**, *3*, 1032.
[52] O. M. Eggenberger, C. Ying, M. Mayer, *Nanoscale* **2019**, *11*, 19636.
[53] X. Kan, C. Wu, L. Wen, L. Jiang, *Small Methods* **2022**, *6*, 2101255.
[54] A. Arima, M. Tsutsui, T. Washio, Y. Baba, T. Kawai, *Anal. Chem.* **2021**, *93*, 215.
[55] F. Wang, C. Zhao, P. Zhao, F. Chen, D. Qiao, J. Feng, *Nat. Commun.* **2023**, *14*, 2895.
[56] M. Tsutsui, K. Yokota, A. Arima, T. Washio, Y. Baba, T. Kawai, *Small Methods* **2021**, *5*, 2100542.
[57] J. Yang, T. Pan, Z. Xie, W. Yuan, H.-P. Ho, *Nat. Commun.* **2024**, *15*, 5132.

